Understanding Interfaces in AlScN/GaN Heterostructures

Isabel Streicher, Stefano Leone, Meiling Zhang, Taoufik Slimani Tlemcani, Micka Bah, Patrik Straňák, Lutz Kirste, Mario Prescher, Ali Yassine, Daniel Alquier, et al.

ADVANCED FUNCTIONAL MATERIALS
www.afm-journal.de

Understanding Interfaces in AlScN/GaN Heterostructures

Isabel Streicher, Stefano Leone,* Meiling Zhang, Taoufik Slimani Tlemcani, Micka Bah, Patrik Straňák, Lutz Kirste, Mario Prescher, Ali Yassine, Daniel Alquier, and Oliver Ambacher*

Aluminum scandium nitride barrier layers increase the available sheet charge carrier density in gallium nitride-based high-electron-mobility transistors and boost the output power of high-frequency amplifiers and high voltage switches. Growth of AlScN by metal-organic chemical vapor deposition is challenging due to the low vapor pressure of the conventional Sc precursor Cp_3Sc, which induces low growth rates of AlScN and leads to thermally-induced AlScN/GaN-interface degradation. In this work, novel Sc precursors are employed to reduce the thermal budget by increasing the growth rate of the AlScN layer. The AlScN/GaN interfaces are investigated by high-resolution X-ray diffraction, high-resolution transmission electron microscopy, time-of-flight secondary ion mass spectrometry, capacitance–voltage, current–voltage and temperature-dependent Hall measurements. Linearly graded interlayers with strain-induced stacking faults, edge, and screw dislocations form at the AlScN/GaN interface at growth rates of 0.015 nms^{-1}. Growth rates of 0.034 nms^{-1} and higher allow for abrupt interfaces, but a compositional grading in the barrier remains. Homogeneous barrier layers can be achieved at growth rates of 0.067 nms^{-1} or by growing an AlN interlayer. The electrical properties of the heterostructures are sensitive to Sc accumulations at the cap/barrier interface, residual impurities from precursor synthesis, and surface roughness. This study paves the way for high-performing devices.

1. Introduction

High-power and high-frequency electronics are the foundation of modern societies. Demand for efficient electric vehicles increases the interest in high-power transistors capable of switching large currents, while the development of 6G mobile networks require increased power at high frequency and large bandwidths. These requirements are met by AlGaN/GaN high-electron-mobility transistors with their high power density at high frequencies (1 W per chip at 71.84 GHz)[1–4] and at the same time high breakdown voltages (above 1 kV).[5] Thanks to heteroepitaxial growth on substrates such as silicon carbide, sapphire or silicon,[6–8] devices are already established on the market for both applications.[1,5,9] However, the controllable currents are limited by the sheet charge carrier density n_s in the 2D electron gas (2DEG) confined at the AlGaN/GaN interface. AlN/GaN transistors provide higher n_s but suffer from the low critical thickness of 5 nm of AlN on GaN that causes short channel effects.[10] Innovative piezoelectric materials such as ε-Ga_2O_3 are predicted to enhance the electron density of two-dimensional-electron-gas (2DEG) confined at the interface with GaN, but their growth presents severe challenges.[11,12] In contrast, the AlScN/GaN system can be the perfect match for both high-power and high-frequency applications. The high bandgap and intrinsically high spontaneous polarization of AlScN compared to GaN allow for high n_s in the 2DEG formed in the GaN channel, close to the AlScN/GaN interfaces.[13–15] An *a* lattice parameter matching to GaN allows for the growth of barriers free of misfit strain and resulting misfit dislocations. Critical thickness limitations are thus overcome. Furthermore, the n_s is not affected by piezoelectric contributions to the total polarization, which limit the n_s of AlGaN/GaN heterostructures to the 10^{12} cm^2 range.[16] In fact, AlScN/GaN

I. Streicher, S. Leone, P. Straňák, L. Kirste, M. Prescher
Fraunhofer Institute for Applied Solid State Physics IAF
Tullastrasse 72, 79108 Freiburg, Germany
E-mail: isabelmariastreicher@gmail.com;
stefano.leone@iaf.fraunhofer.de

The ORCID identification number(s) for the author(s) of this article can be found under https://doi.org/10.1002/adfm.202403027

DOI: 10.1002/adfm.202403027

M. Zhang, T. S. Tlemcani, M. Bah, D. Alquier
GREMAN UMR 7347, CNRS, Université de Tours
INSA Centre Val de Loire
16 rue Pierre et Marie Curie, 37071 Tours, France

A. Yassine, O. Ambacher
Gips-Schüle Chair for Power Electronics
Institute for Sustainable Systems Engineering (INATECH)
University of Freiburg
Emmy-Noether-Strasse 2, 79110 Freiburg, Germany

allows for approximately 4.5 times higher n_s than AlGaN/GaN heterostructures.[17] It is currently under discussion whether the lattice matching occurs at a Sc concentration of 18 %, a value determined by calculations,[18,19] or at 11 %, as suggested by recent experimental studies.[20] This is crucial since strain and resulting misfit dislocations reduce the lifetime of devices considerably.[21]

To date, AlScN/GaN heterostuctures are grown by molecular beam epitaxy (MBE),[13,22,23] and metal-organic chemical vapor deposition (MOCVD).[8,24–27] While MBE-growth allows for well-defined, atomically sharp interfaces, MOCVD-grown heterostructures are oftentimes characterized by interfacial diffusion present in high-growth temperature processes such as those for GaN and SiC, which may be mitigated by reducing the growth temperature, which eventually leads to challenges in controlling the structural characteristics of the material.[28–31] However, MOCVD is the preferred growth technique in industry thanks to the high throughput, low maintenance costs, and fast growth processes. Single crystalline, ferroelectric MOCVD-grown AlScN was recently demonstrated.[32] Growth of AlScN by MOCVD is challenging due to the low vapor pressure of the conventional Sc precursor tris-cyclopentadienyl-scandium Cp_3Sc and was not possible,[33,34] until a gas supply system for temperatures up to 155 °C was developed.[24] The solid Cp_3Sc delivers molar flows in the range of few $molmin^{-1}$ and Sc incorporation into the growing layer increases with growth temperature and fluctuates from run to run. The extremely low growth rate of 0.006 nms^{-1} leads to a very high thermal budget that promotes the diffusion of Al atoms into the GaN channel. This and strain related effects cause graded AlGaN interlayer formation, as we reported recently.[27] These interlayers lead to a broadening of the potential well at the barrier/channel interface across the whole graded area. This is not necessarily detrimental to devices, graded AlGaN channels were even reported to improve RF device linearity,[35,36] but it can be assumed that alloy scattering increases and reduces 2DEG mobility and thus device switching speed. An AlN interlayer can be inserted between channel and barrier in order to increase interface abruptness even at extremely low barrier growth rates. Binary AlN interlayers are reported to eliminate alloy scattering in both AlGaN/GaN[37] and AlScN/GaN heterostructures,[38] and reduce interface roughness scattering.[39] Furthermore, they are employed to increase interface abruptness and can act as diffusion barriers.[40]

Recently, we reported that it is possible to increase the growth rate to 0.015 nms^{-1} by using bis- methylcyclopentadienyl - scandium-chloride $(MCp)_2ScCl$ as Sc precursor.[8] The increased vapor pressure allows for higher molar flows, higher growth rates and improved run-to-run stability. The presence of Cl in the precursor did not cause any incorporation of Cl in solid phase, as similarly observed in the Cl-assisted CVD growth of SiC.[41–47] AlScN/GaN HEMTs with a saturation drain current density I_{sat} of 1.7 Amm^{-1}, a power-added efficiency PAE of 48.9% and an output power P_{out} of 8.4 Wmm^{-1} at 30 GHz were demonstrated.[48] This combination of PAE and P_{out} exceeds that reported for MBE-grown AlScN/GaN HEMTs so far.[14,49–52]

In this work, the novel Sc precursors with enhanced vapour pressures, bis(ethylcyclopentadienyl) (N,N'-bis (dimethylamino) acetamidinato) scandium $(EtCp)_2Sc(bdma)$ and bis (ethylcyclopentadienyl) (di-tert-butyl-triazenido) scandium $(EtCp)_2Sc(dtbt)$, are employed to increase the growth rate to around 0.034 and 0.067 nms^{-1}, respectively. We focus on understanding how highly abrupt interfaces in MOCVD-grown AlScN/GaN heterostructures can be obtained by MOCVD and how the interfaces affect the structural and electrical characteristics of the AlScN/GaN heterostructures. The degradation mechanisms that lead to the formation of graded Al(Ga,Sc)N interlayers at the barrier/channel interface when extremely low growth rates are employed are examined in detail. High-resolution X-ray diffractometry (HRXRD), time-of-flight secondary ion mass spectrometry (ToF-SIMS) and high-resolution transmission electron microscopy (HRTEM) in combination with capacitance–voltage (*C–V*), current–voltage (*I–V*) and temperature-dependent Hall measurements are employed to evaluate structural quality, as well as electrical performance of the heterostructures. The role of AlN interlayers at low and high growth rates is evaluated as well.

2. Experimental Section and Simulation

A close-coupled showerhead MOCVD reactor equipped with a proprietary setup for epitaxial growth with low - vapor pressure precursors, described in detail by Leone et al.[24,53], was used for the growth of AlScN/GaN heterostructures. A mass flow controller installed upstream of the Sc bubbler and a pressure gauge for monitoring the pressure at the bubbler outlet allows for controlling the molar flow. Novel Sc precursors developed by Dockweiler Chemicals GmbH[54] were employed to increase the molar flow and, with it, the growth rate of the AlScN layer. With bis-methylcyclopentadienyl- scandiumchloride $(MCp)_2ScCl$, the growth rate was doubled with respect to the one achieved with the conventional precursor triscyclopentadienylscandium Cp_3Sc, at a source temperature of 155 °C. With bis (ethylcyclopentadienyl) (N,N'-bis (dimethylamino) acetamidinato) scandium $(EtCp)_2Sc(bdma)$, the growth rate was doubled once more to 0.034 nms^{-1} at a reduced source temperature of 100 °C. At the same source temperature, bis (ethylcyclopentadienyl) (di-tert-butyl-triazenido) scandium $(EtCp)_2Sc(dtbt)$ was employed for a growth rate as high as 0.067 nms^{-1}, one order of magnitude above the growth rate achieved with Cp_3Sc. The vapor pressure of the novel chemicals needs yet to be determined and thus the exact molar flow remains unknown. The thermal budget the growing structure is exposed to is thus reduced significantly. The Al, Ga, Si, and N sources were trimethylaluminum (TMAl), trimethylgallium (TMGa), silane (SiH_4) and ammonia (NH_3), respectively. The carrier gas was hydrogen. The epitaxial layers were grown on 4-inch substrates of either c-plane Al_2O_3 or semi-insulating 4H-SiC. Like in our previous works,[8,25–27] a low-temperature GaN on Al_2O_3 or AlN nucleation layer on 4H-SiC, a Fe-doped GaN channel layer to compensate background donor concentrations thanks to its deep-levels introduced in materials such as GaN and SiC,[55,56] and a non-intentionally doped GaN as channel and channel layer were grown. 10 to 15 nm-thick AlScN barriers were grown at 1100 °C with the Sc precursors $(MCp)_2ScCl$, $(EtCp)_2Sc(bdma)$ and $(EtCp)_2Sc(dtbt)$ without intentional interlayers in order to understand the formation of interface grading in relation to the thermal budget generated by the growth time. A sample grown with Cp_3Sc at a growth rate of 0.006 nms^{-1} was used as benchmark.[27]

Table 1. Summary of the samples studied in this work listed in order of decreasing growth rate without and with AlN interlayer. The employed Sc precursors, growth temperatures, growth rates, and substrates are listed as well as the AlScN barrier thicknesses th and SiN_x cap thicknesses determined by HRXRD and XRR, the x_{Sc} determined by (ToF-)SIMS, surface roughness RMS determined by AFM and average R_{sh}, n_s, and obtained across the 4 inch wafers by contactless Hall measurements. The samples grown with Cp_3Sc at a growth rate of 0.006 nms^{-1} were discussed in detail in our previous work,[27] and are used as benchmark.

GR [nms^{-1}]	Sc precursor	T [°C]	IL	Substrate	th [nm]	SiN_x [nm]	x_{Sc} [–]	RMS [nm]	R_{sh} [Ω sq^{-1}]	n_s [10^{13} cm^{-2}]	[$cm^2(Vs)^{-1}$]
0.067	$(EtCp)_2Sc(dtbt)$	1100	no	Al_2O_3	11.1	21.5	8.6	0.30	273 ± 4 %	2.50 ± 3 %	914 ± 4 %
0.034	$(EtCp)_2Sc(bdma)$	1100	no	Al_2O_3	15.3	9.8	4 – 8.0	1.04	303 ± 5 %	2.55 ± 8 %	813 ± 7 %
0.015	$(MCp)_2ScCl$	1100	no	4H-SiC	10.5	3.4	8.0	0.53	280 ± 1 %	2.97 ± 3 %	751 ± 3 %
0.006	Cp_3Sc	1100	no	4H-SiC	14.1	7.5	–	0.41	326 ± 2 %	2.25 ± 12 %	861 ± 10 %
0.067	$(EtCp)_2Sc(dtbt)$	1100	yes	Al_2O_3	11.3	13.9	8.2	0.43	265 ± 2 %	2.71 ± 2 %	868 ± 3 %
0.006	$(MCp)_2ScCl$	800	yes	Al_2O_3	15.5	1.1	8.0	7.82	239 ± 2 %	4.20 ± 2 %	622 ± 4 %
0.006	Cp_3Sc	1000	yes	4H-SiC	8.9	2.7	2 – 8.5	0.28	242 ± 7 %	3.25 ± 10 %	802 ± 6 %
0.006	Cp_3Sc	1000	no	4H-SiC	11.0	2.8	4.2	0.23	263 ± 1 %	2.52 ± 13 %	957 ± 14 %

Furthermore, the effect of AlN interlayers on vertical Sc distribution and interface abruptness was investigated and related to the Sc molar flow, growth temperature and growth rate. Binary AlN interlayers can be employed to reduce alloy scattering because they spatially separate the 2DEG from the ternary barrier and improve the interface abruptness, as shown in the previous work.[27]

The highly negative standard redox potential of Sc makes it very susceptible to oxidation and indeed considerable surface oxidation was reported.[57] Consequently, the surface of all heterostructures got passivated in situ with SiN_x. The samples discussed in this work are listed in **Table 1**.

Atomic force microscope (AFM) in tapping mode was used to examine the surface morphology and determine the surface roughness of the grown structures as the root mean square (RMS) average. High-resolution X-ray diffractometry (HRXRD) Θ/2Θ-scans of the 0002, 0004, and 0006 reflections combined with X-ray reflectometry (XRR) was used to determine the barrier and cap layer thickness. The growth rates were determined by dividing the HRXRD barrier thickness in nanometers (nm) by the growth time in seconds (s). Reciprocal space mapping (RSM) of the $\overline{1}\overline{1}24$-reflection was employed to confirm that the AlScN barrier was coherently strained to the underlying GaN.

Time-of-flight secondary ion mass spectrometry (ToF-SIMS) was employed for chemical composition analysis. The depth profiles were obtained in a dual beam mode using a sputter beam of 1 keV Cs^+ ions. A primary beam of 30 keV $^1Bi^+$ ions was used for the crater analysis. The $AlCs^+/ScCs^+$ signal ratio was compared to that of magnetron-sputtered AlScN reference samples to determine the Sc concentration. The reference samples were previously calibrated by energy elastic recoil detection analysis (ERDA).[58] Oxygen and carbon impurity concentrations were not quantified due to the lack of standards, however, their signal intensities were compared qualitatively.

High-resolution transmission electron microscopy (HRTEM) was employed to investigate the active layers' structural quality and crystallographic structure. Imaging along both the $\langle 1\overline{1}00\rangle$ and $\langle 11\overline{2}0\rangle$ zone axis were performed to investigate on the structural quality and presence of defects such as stacking faults. The $\langle 1\overline{1}00\rangle$ zone axis allowed for the identification of misfit dislocations, while the $\langle 11\overline{2}0\rangle$ zone axis allowed for the discrimination of wurtzite and zincblende stacking.

Capacitance–voltage (*C–V*) measurements were performed to confirm the presence of a 2DEG in the grown heterostructures and to identify parasitic capacitances caused by compositional gradings and impurity incorporation. The charge carrier distribution was derived using the formula proposed by Ambacher et al.[59] The AlN value of 8.5[60] was taken as effective relative dielectric permittivity ε_{eff} of both the SiN_x cap and the $Al_{1-x}Sc_xN$ barrier. With the same mercury-probe set-up, current–voltage (*I–V*) measurements of a mercury Schottky contact were performed in order to compare the variation of leakage currents in the reversed biased direction for the different layers. Schottky gate leakage currents fatal to devices could be anticipated with these measurements.

With a contactless mobility mapper, eddy-current sheet resistance and contactless Hall measurements were carried out with 17 measurement points evenly distributed across the four-inch wafers. The average values of the sheet resistance (R_{sh}), sheet charge carrier density (n_s), and electron mobility (), including standard deviations, are given in Table 1. The standard deviations across the wafers decreased notably with using the novel Sc precursors $(MCp)_2ScCl$, $(EtCp)_2Sc(bdma)$ and $(EtCp)_2Sc(dtbt)$ with enhanced vapour pressures compared to wafers grown with Cp_3Sc. Temperature-dependent Hall measurements from 7 K to room temperature were performed with alloyed Ti/Al/Au-based contacts. The behavior of with temperature was evaluated by calculating the individual mobility contributions of different scattering mechanisms with the equations given by Jena.[61,62] These were derived from the Boltzmann transport equation using Fermi's golden rule for the scattering rates. The extrinsic, temperature-dependent mechanisms, polar optical phonon (POP), and acoustic phonon (AP) scattering were considered, as well as the intrinsic, temperature-independent alloy disorder (AD), background residual impurity (BRI) and interface roughness (IR) scattering mechanisms. The total mobility was calculated according to the Matthiesen rule as the sum of the individual contributions of each considered scattering mechanism.

The conduction band edge and the theoretical charge carrier distributions shown in this work were calculated with the 1D Schrödinger-Poisson equation solver nextnano^{++}.[63]

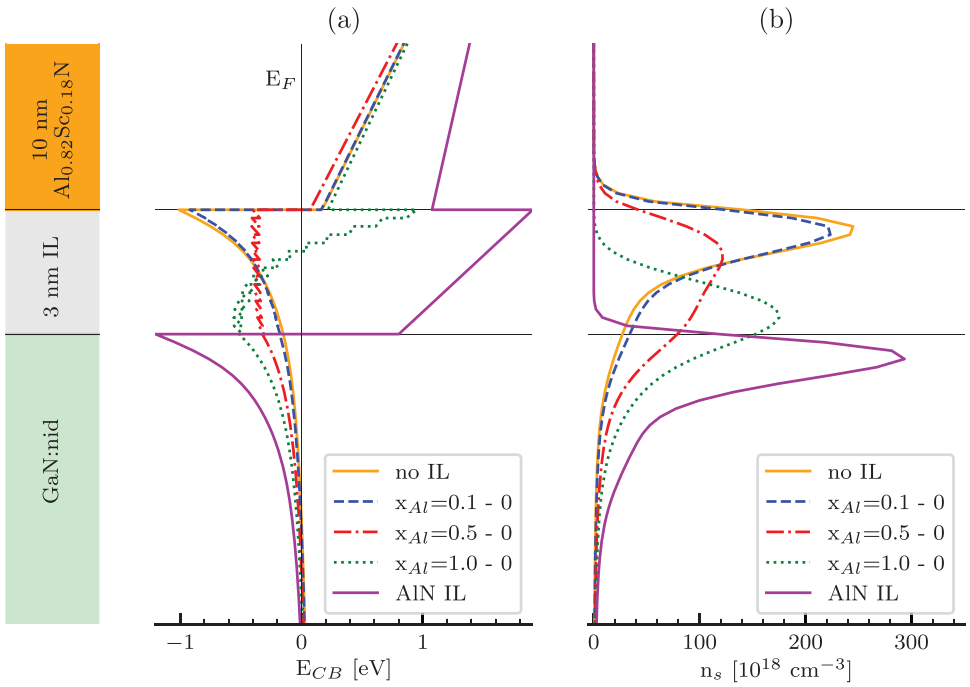

Figure 1. a) Conduction band edges and b) charge carrier distributions for linearly graded interlayers (IL) show the broadening and relocation of the 2DEG peak for different concentration gradients. Simulated using the 1D Schrödinger-Poisson equation solver nextnano.[63] The n_s are 4.32, 4.32, 4.26, 4.35, and 4.90 × 10^{13} cm^{-2} for no IL, $x_{Al} = 0.1 - 0$, $x_{Al} = 0.5 - 0$, $x_{Al} = 1.0 - 0$ and an AlN IL, respectively.

3. Results and Discussion

Low growth rates at high growth temperatures lead to a high thermal budget and thus favor interface degradation. The extremely low vapor pressure of the Sc precursor Cp_3Sc makes the incorporation of Sc challenging and limits the growth rate to a maximum of 0.006 nms^{-1}. We reported significant interface degradation by the formation of several nm-thick, linearly graded AlGa(Sc)N interlayers in our previous work.[27] Linearly graded interfaces lead to a broadening of the potential well, relocation of the 2DEG peak, and a loss in carrier confinement of the 2DEG. This is shown in **Figure 1** for linear gradings with different slopes. The broadening of the 2DEG is less pronounced in very steep and very shallow gradings. Increased alloy scattering can be expected since the electron gas is located in the ternary/quaternary region for all scenarios. Binary AlN interlayers spatially separate the 2DEG from the ternary barrier and reduce alloy scattering. Furthermore, the high bandgap of AlN increases the potential barrier, and the increased polarization discontinuity further enhances the n_s.

3.1. Growth Rate and Interlayer Formation

High growth temperatures (>1100 °C) favor interdiffusion of atoms across the AlScN/GaN interface but reduce the oxygen and carbon impurity incorporation drastically with respect to growth at low temperatures.[25] Growth rate enhancement is the only way to reduce the thermal budget when the growth temperature is high. Three samples were grown without a nominal interlayer at 1100 °C with increasing growth rates of 0.015, 0.034, and 0.067 nms^{-1} using the Sc precursors $(MCp)_2ScCl$, $(EtCp)_2Sc(bdma)$ and $(EtCp)_2Sc(dtbt)$, respectively. A reference sample grown at the same temperature with the conventional Sc precursor Cp_3Sc at a growth rate of 0.006 nms^{-1} is used as benchmark. The growth temperature and cooling process were identical for all samples. In **Figure 2**, HRXRD Θ/2Θ-scans are shown. The thicknesses determined from these scans in combination with XRR are listed in Table 1. With increasing growth rate, the AlScN peak in the HRXRD Θ/2Θ-scans of the 0002, 0004, and 0006 reflections gets more pronounced. A well-defined AlScN-related peak and a high number of thickness fringes are an indicator for the interface abruptness but also scales with the layer thickness. While the peak of the 14.1 nm-thick AlScN barrier in the benchmark sample (0.006 nms^{-1}) is hard to identify behind the AlN nucleation layer peak, the layer grown with doubled growth rate (0.015 nms^{-1}) is clearly visible even though the barrier is only 10.5 nm-thick. The 15 nm-thick barrier grown with again doubled growth rate of 0.034 nms^{-1} features a very well pronounced barrier peak and an increased number of thickness fringes. The AlScN peak of the only 11.1 nm-thick barrier grown with the highest growth rate of 0.067 nms^{-1} is equally very well defined. The lower number of thickness fringes compared to the other samples is attributed to the lower thickness compared to the sample grown at a growth rate of 0.034 nms^{-1} and to the about one order of magnitude higher amount of threading dislocations in samples grown on Al_2O_3 with respect to samples grown on 4H-SiC.

The chemical composition and elemental depth profiles were analyzed with ToF-SIMS, as shown in **Figure 3**. Backdiffusion of Al and Sc into the GaN channel is observed in all samples, starting roughly from the interface of barrier, including interlayer, and channel determined by HRXRD. It follows a classical

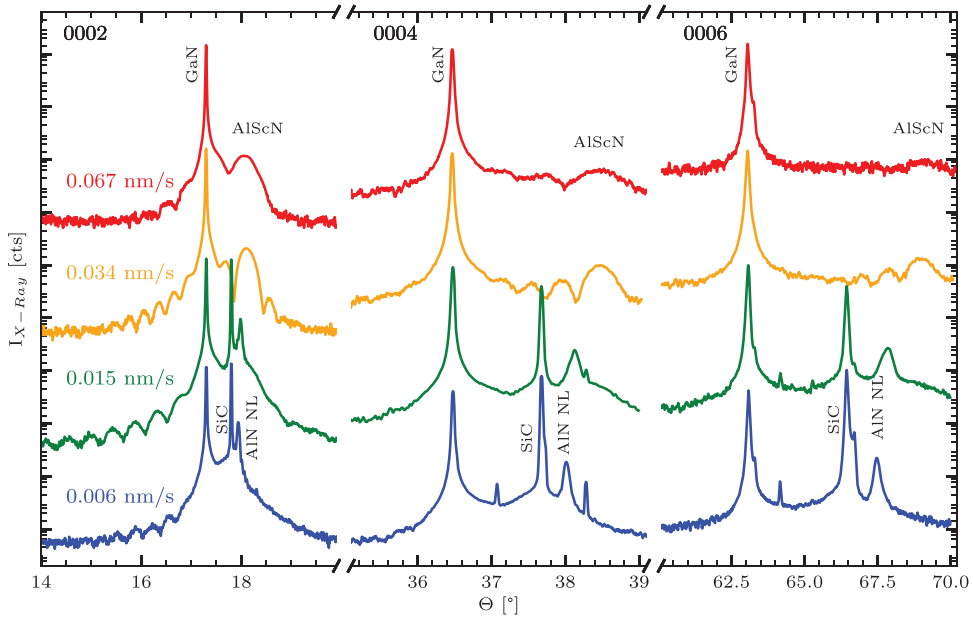

Figure 2. HRXRD Θ/2Θ-scans of the 0002, 0004, and 0006 reflections of AlScN/GaN heterostructures grown at 1100°C with growth rates of 0.006 and 0.015 nms^{-1} on 4H-SiC, as well as 0.034 and 0.067 nms^{-1} on Al_2O_3. The precursors Cp_3Sc, $(MCp)_2ScCl$, $(EtCp)_2Sc(bdma)$, and $(EtCp)_2Sc(dtbt)$ were employed, respectively.

diffusion profile and drops to the signal intensity of 10^{-1} within approximately 14 nm from the barrier/channel interface. In contrast, the presence of linear compositional gradings relates with the growth rate. In Figure 3a, we show the sample grown with Cp_3Sc at a growth rate of 0.006 nms^{-1}, that we presented in our previous work, as reference.[27] Note that this sample was grown at 1000 °C. The $GaCs^+$ signal exhibits a very shallow linear grading from the barrier/channel interface toward the cap and tails off only in the uppermost part of the barrier. The $ScCs^+$ signal increases from the barrier/channel to the cap/barrier interface with very low signal intensities. With HRTEM, we found that the top AlScN layer is only 2.7 nm thick and contains 4.2 % Sc.[27] The sample grown with a doubled growth rate of 0.015 nms^{-1} features an approximately 7 nm-thick linearly graded quarternary interlayer in which the $ScCs^+$ signal increases linearly toward the cap (Figure 3b). The $ScCs^+$ signal plateaus eventually, and the $GaCs^+$ drops by almost two orders of magnitude, giving rise to a 3.5 nm AlScN barrier layer. In this layer, the Sc concentration was determined to 8.0 %. When the growth rate is increased to 0.034 nms^{-1}, the linearly graded AlGaScN interlayer disappears (Figure 3c). The interface between AlScN and GaN seems abrupt. The $ScCs^+$ signal increases linearly across the whole barrier layer toward the cap. The $GaCs^+$ signal intensity is very low and further decreases linearly. The barrier can be interpreted as a linearly graded AlScN layer with the Sc fraction increasing from 4 to 8 %. A homogeneous barrier is achieved when the growth rate is further increased to 0.067 nms^{-1} (Figure 3d). Graded interlayers lead to a broadening of the potential well at the heterojunction interface. This broadens the 2DEG distribution into the third dimension across the graded interlayer, presumably favoring alloy scattering. In fact, with increasing growth rate from 0.015 to 0.034 to 0.067 nms^{-1} and thus increasing interface abruptness, the electron mobility increases from 751 ± 3 % to 813 ± 7 % to 914 ± 4 % $cm^2/(Vs)$ in contactless Hall measurements.

3.1.1. Structural Defects in Graded Layers

The linearly graded AlGaScN layer that characterizes the transition from the GaN channel to the AlScN barrier is examined by HRTEM analysis along the $\langle 1\bar{1}00 \rangle$ zone axis shown in **Figure 4**. This axis allows for the visualization of misfit dislocations. The AlScN barrier layer features accurate atomic planes. In contrast, the graded AlGaScN interlayer contains a number of defects causing contrast fluctuations, that start from the interface to the GaN channel layer, as can be seen in Figure 4a. With the help of the Bragg filtered image shown in Figure 4b, an edge dislocation (red, green) and a screw dislocation (orange) can be identified. In the heteroepitaxial growth of lattice-mismatched layers, the formation of extra halfplanes indicates that local strain relaxation takes place and leads to plastic deformation. In fact, the 8.0 % Sc determined in the topmost part of the Sc-containing section of the heterostructures is far from the lattice-matched condition, which is expected to occur at 18.0 %, or according to more recent studies, around 11.0 %. In literature, defect generation by strain relaxation was observed, for example, in GaN/AlN,[64] AlGaN/GaN,[65] AlInN/GaN,[66] and InGaN/GaN heterostructures.[67,68] These dislocations can act as scatterers for the electron gas, especially given that the 2DEG is expected to spread across graded interlayers. In Figure 4c, a type-I stacking fault (I_1) with an ABABCBCB...CBABAB stacking located in the interlayer is shown. Several of these stacking faults can be found in different parts of the interlayer, in the proximity of screw dislocations. According to literature, I_1 stacking faults are confined by sessile Frank–Shockley partial dislocations and are intrinsic

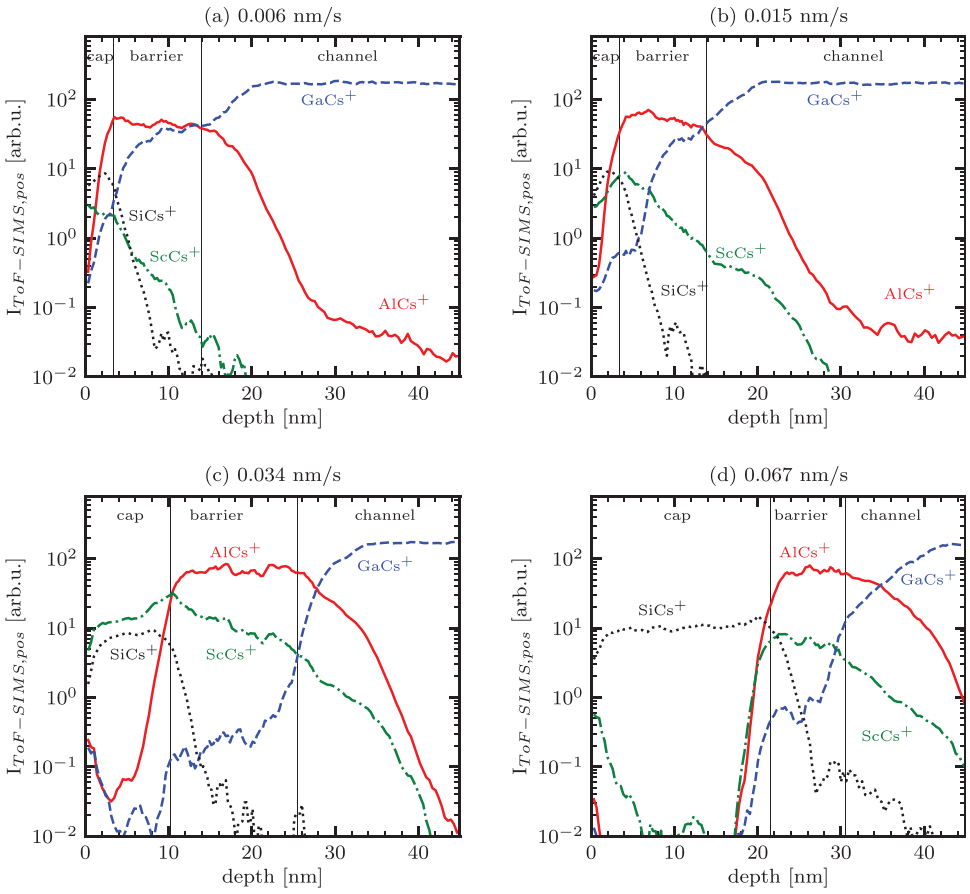

Figure 3. ToF-SIMS depth profiles for samples grown with growth rates of a) 0.006 nms^{-1} (benchmark sample from),[27] b) 0.015 nms^{-1} using $(MCp)_2ScCl$, c) 0.034 nms^{-1} using $(EtCp)_2Sc(bdma)$ and d) 0.067 nms^{-1} using $(EtCp)_2Sc(dtbt)$ as Sc precursor. Obtained signals were normalized to NCs^+ signal to minimize the matrix effect. The oxidation layer developed on the surface of the SiN cap in (d) interferes with the $ScCs^+$ signal, and the signal in the first 10 nm belongs to $^{28}SiOHCs^+/^{29}SiOCs^+$. The $AlCs^+$ signal tail visible below approximately 7×10^{-2} arb. u. in (a) and (b) is a measurement artifact attributed to the background signal generated by sputter gun ions. The SiN_x and barrier including interlayer thicknesses determined by HRXRD are indicated by vertical lines.

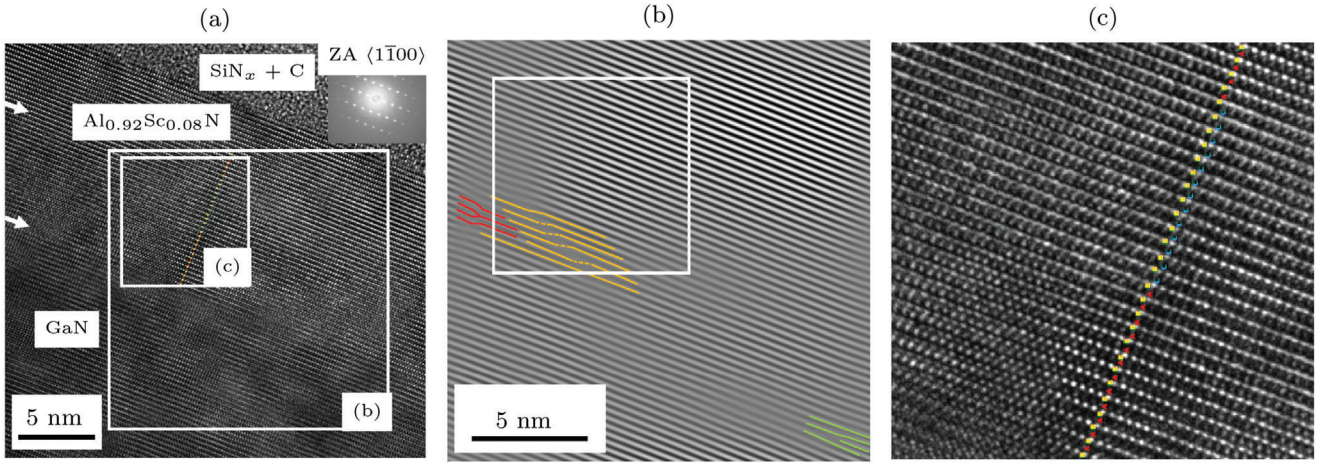

Figure 4. a) HRTEM image obtained along the ⟨1$\bar{1}$00⟩ zone axis. b) Bragg filtered image and c) zoom to a type I stacking fault.

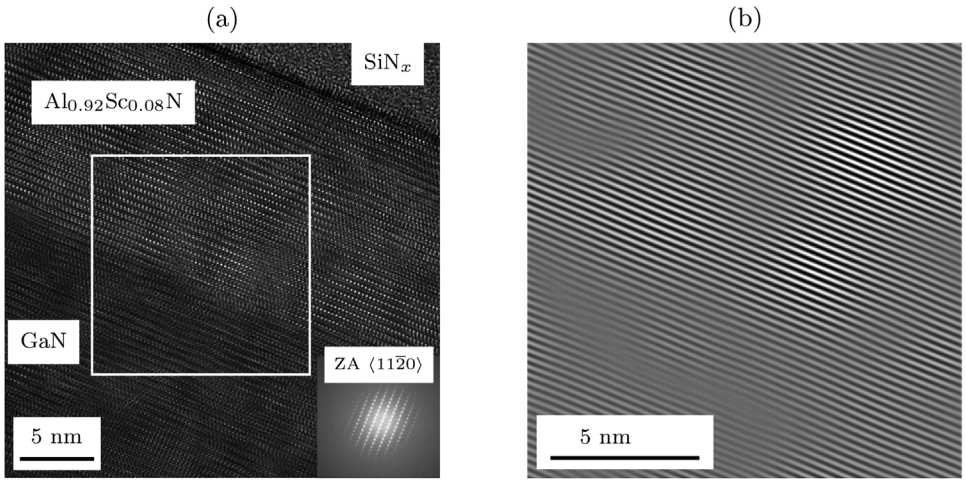

Figure 5. a) HRTEM image obtained along the $\langle 11\bar{2}0\rangle$ zone axis and the respective b) Bragg filtered image.

in character. Stampfl et al.[69] do not see a relation to strain relaxation but to growth. Double positioning or local deviations from stoichiometry are reported to cause I_1 stacking faults,[66–68,70] but also the collapse of atomic layers into lattice vacancies or voids during the cooling process.[71] Other typical defects that have been reported close to the barrier/channel interface of AlGaN/GaN heterostructures are type- II stacking faults (I_2) that locally introduce zincblende layers.[72] In the given crystallographic direction, they cannot be identified. Given that the formation enthalpy of the wurtzite and the zincblende phase are very close for low Sc concentrations,[73,74] they could be present.

These findings suggest that the graded AlScN barrier of the sample grown at growth rate of 0.034 nms^{-1} might contain strain-related defects since a compositional grading is present and the same cooling procedure was applied. However, in the HRTEM image along the $\langle 11\bar{2}0\rangle$ zone axis, as presented in **Figure** 5a, no structural defects are observed. This zone axis allows for the visualization of type II stacking faults but none are present. The interface of the Sc-containing layer and the GaN can be distinguished unambiguously thanks to the clear contrast difference. The Bragg filtered image in Figure 5b shows well-aligned atomic planes. The contrast variation in the HRTEM contrast and blurry zones in the Bragg-filtered image of the AlScN layer, especially near the interface, can be attributed to remnant strain caused by the lattice mismatch to the underlying GaN layer.

3.1.2. Electrical Performance

Structural defects or impurity doping can lead to leakage currents that can affect device performance negatively. The *I–V* measurements of the samples grown with a growth rate of 0.015 and 0.067 nms^{-1} show the expected Schottky behavior in **Figure** 6. Current is conducted in the forward direction and blocked in the reverse direction. The leakage current flow at negative voltages is in the high 10^{-7} and low 10^{-8} A range, respectively.

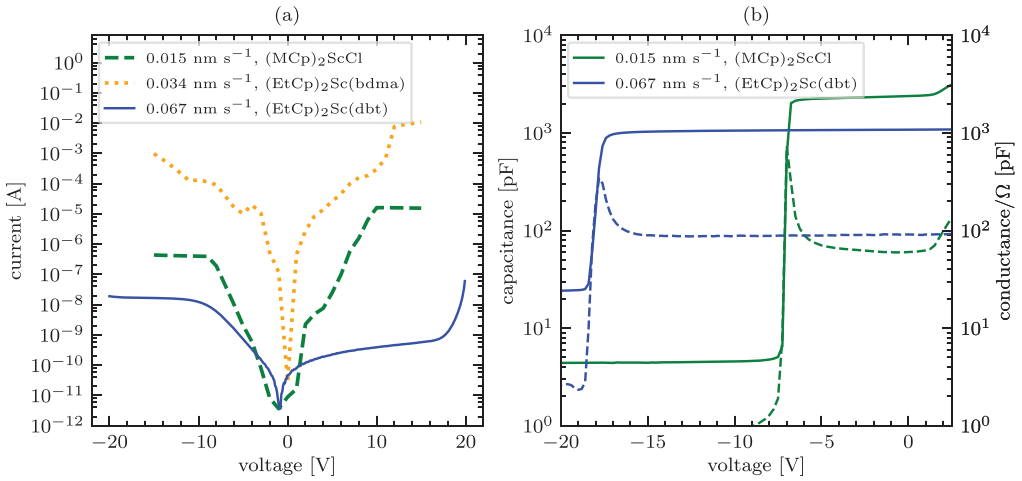

Figure 6. a) Current–voltage (*I–V*) profiles of the samples grown at growth rates of 0.015, 0.034, and 0.067 nms^{-1} with $(MCp)_2ScCl$, $(EtCp)_2Sc(bdma)$ and $(EtCp)_2Sc(dtbt)$ as Sc precursors and b) capacitance–voltage (*C–V*) profiles of the samples grown with $(MCp)_2ScCl$ and $(EtCp)_2Sc(dtbt)$.

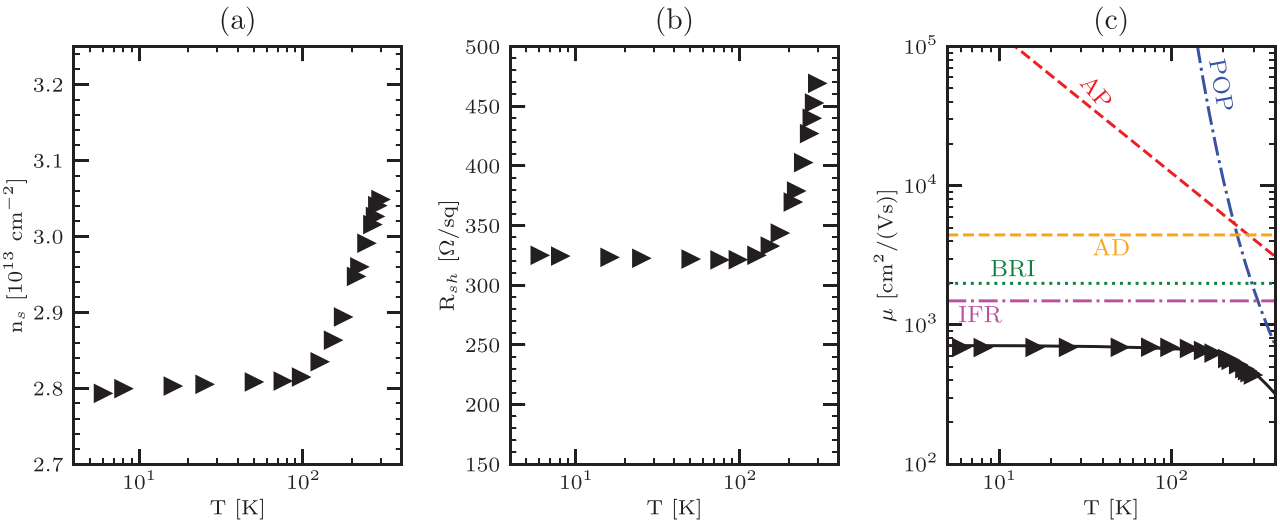

Figure 7. Temperature-dependent Hall measurement on the sample grown with a growth rate of 0.034 nms^{-1} with $(EtCp)_2Sc(bdma)$ as Sc precursor. Experimentally determined a) n_s, b) R_{sh}, and c) from 7 K to room temperature. Calculated POP, AP, AD, BRI, and IR scattering limited mobilities are indicated. The total mobility calculated according to the Matthiesen rule fits the experimental data.

Thereby, the homogeneous barrier and abrupt, interlayer-free interface feature the lower leakage current. The sample grown with a growth rate of 0.034 nms^{-1} shows very high leakage currents in the range of 10^{-3} to 10^{-2} A. For this sample, it was not possible to measure a *C–V* curve, while those of the other two samples are shown in Figure 6b. The presence of 2DEGs is confirmed by the abrupt capacitance drop across several orders of magnitude and the corresponding conductance peaks. The very deep capacitance drop might be supported by acceptor traps in the channel layer, where the 2DEG resides. The threshold voltage V_{th} shift from −7 to −19 V can be attributed to the SiN_x cap layer thickness: The sample grown with $(MCp)_2ScCl$ has a 3.4 nm-thick cap and the one grown with $(EtCp)_2Sc(dtbt)$ a 21.5 nm-thick cap. The capacitance is constant above the V_{th} for the sample with the homogeneous and the abrupt interface grown at a growth rate of 0.067 nms^{-1}. The sample grown at 0.015 nms^{-1} with the graded AlGaScN interlayer shows a parasitic capacitance increase at positive voltages. This hints at the presence of electrons in the barrier or in parts of the barrier. In fact, graded interlayers can spread the 2DEG into three dimensions, as shown earlier in Figure 1. Another explanation could be the presence of donor impurities. However, SIMS measurements (not shown) suggest that oxygen and carbon levels are lower for layers grown with Cp_3Sc and $(MCp)_2ScCl$, and higher in layers grown with $(EtCp)_2Sc(bdma)$ and $(EtCp)_2Sc(dtbt)$, respectively. Consequently, if the parasitic capacitance related to donor impurities, also the sample grown with $(EtCp)_2Sc(dtbt)$ should have featured it. Likewise, the fact that low leakage currents and optimum *C–V* curves were obtained on the layers grown with $(EtCp)_2Sc(dtbt)$, whose impurity concentrations are very similar to those of the layers grown with $(EtCp)_2Sc(bdma)$, suggest that this is not the source of the leaky behavior of the $(EtCp)_2Sc(bdma)$ −sample.

Instead, Sc-rich zones at the surface of the barrier and in/on top of the SiN_x cap of the sample grown with $(EtCp)_2Sc(bdma)$ as Sc precursor, can be held responsible for the high leakage currents observed in *I–V* measurements. They were identified with ToF-SIMS (Figure 3c). ScN is reported to be a degenerate n-type semiconductor,[75] and could contribute to the high leakage current. The origin of these Sc-rich zones was residual Sc in the gas lines that became noticeable only when high molar flows were operated. The issue was solved by purging the gas lines and reducing the gas inlet temperature for the growth of the SiN_x cap. Like this, residual Sc incorporation got successfully suppressed in the heterostructure grown with $(EtCp)_2Sc(dtbt)$ as Sc precursor (Figure 3d).

The temperature-dependent Hall measurement in **Figure 7** shows that the room temperature n_s of 3.06×10^{13} cm^{-2} is decreased by 8 % to 2.80×10^{13} cm^{-2} at around 200 K, remaining stable down to 7 K (Figure 7a). About 0.26×10^{13} cm^{-2} electrons get thermally deactivated. In bulk semiconductors, deactivation is mostly associated with a freeze-out of carriers that are bound to their donor atom. In a 2DEG, the electrons are spatially separated from their donor atom by the built-in electric field across the barrier layer, and the potential barrier is too high to make electrons return to their donor atom when the temperature is decreased. In this case, two interpretations are possible: The 2DEG electrons get trapped in shallow acceptor states induced by carbon impurities in the GaN channel where the 2DEG is located, or bulk donors in the ScN-rich zones on top of the cap freeze out. The R_{sh}, shown in Figure 7b, decreases from a 469 Ω sq^{-1} at room temperature to 325 Ω sq^{-1} at 7K, while, shown in Figure 7c, increases from 436 to 688 cm^{-2} (Vs)$^{-1}$. This behavior is caused by the intrinsic, temperature dependent scattering mechanisms, POP and AD, that limit the room temperature mobility of the 2DEG electrons. At low temperatures (<200 °C), the extrinsic scattering mechanisms AD, BRI, and IFR dominate. The elevated surface roughness with an RMS of 1.04 nm and the high impurity levels make IFR and BRI the dominant mobility-limiting mechanisms at low temperatures.

In contrast to that of the $(EtCp)_2Sc(bdma)$ sample, the temperature-dependent Hall measurement of the sample grown with $(MCp)_2ScCl$ at a growth rate of 0.015 nms^{-1}, shows classical 2DEG behavior. As shown in **Figure 8a**, the n_s remains constant across the whole temperature range. The R_{sh} in Figure 8b

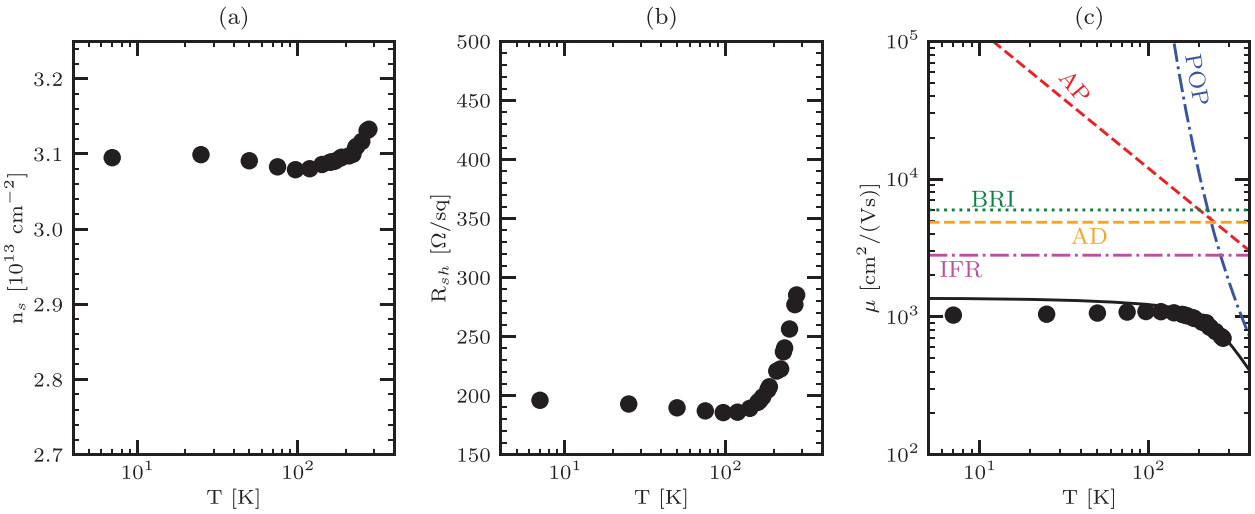

Figure 8. Temperature-dependent Hall measurement on the sample grown with a growth rate of 0.015 nms^{-1} with $(MCp)_2ScCl$ as Sc precursor. Experimentally determined a) n_s, b) R_{sh}, and c) from 7 K to room temperature. Calculated POP, AP, AD, BRI, and IR scattering limited mobilities are indicated. The total mobility calculated according to the Matthiesen rule fits the experimental data.

is 200 Ω sq^{-1} from 7 to 210 K and increases to 290 Ω sq^{-1} at room temperature, while the decreases from 1029 to 697 cm^{-2} (Vs)$^{-1}$ (Figure 8c). Decreased impurity levels reduce the contribution of BRI scattering to the low-temperature mobility. Instead, the graded interlayer leads to AD and IFR even though the surface roughness is low with a RMS of 0.53 nm.

3.2. Intentional AlN Interlayer

The growth of a nominal AlN interlayer can be employed to suppress the formation of linearly graded AlGa(Sc)N interlayers at the interface of the barrier and the channel layer when growing with extremely low growth rates of 0.006 nms^{-1} with Cp_3Sc as Sc precursor.[27] The AlScN-related peak in the HRXRD Θ/2Θ-scans of the 0002, 0004, and 0006 reflections are much more pronounced when an AlN interlayer is grown at otherwise fixed conditions, as illustrated in **Figure 9**. An increase in molar flow by using $(MCp)_2ScCl$ as a Sc precursor while reducing the growth temperature to 800 °C leads to an increased number of thickness fringes and a very well-defined AlScN peak, indicating superior structural quality. Similarly high structural quality is achieved with the increase of growth rate by a factor of ten with the Sc precursor $(EtCp)_2Sc(dtbt)$ at a growth temperature of 1100 °C when the heterostructure is

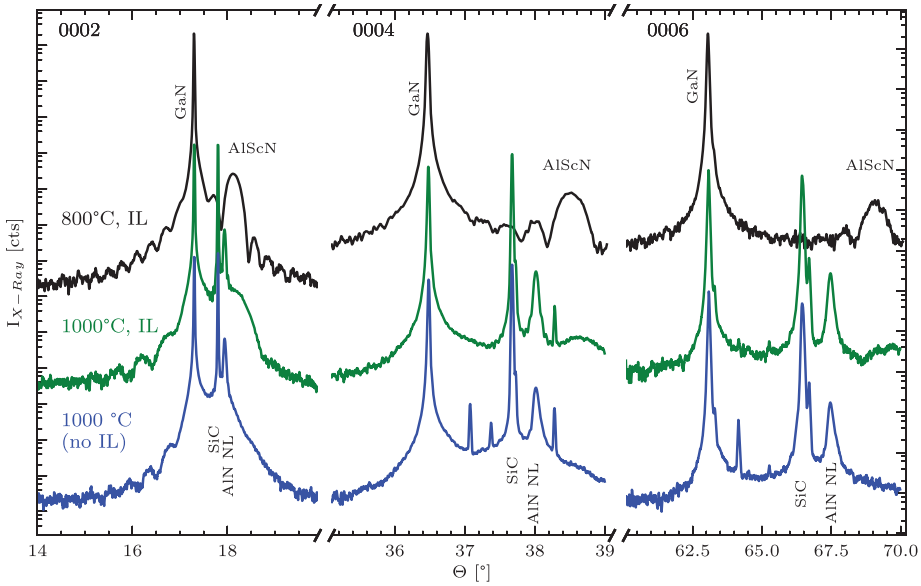

Figure 9. HRXRD Θ/2Θ-scans of the 0002, 0004, and 0006 reflections of AlScN/GaN heterostructures grown with AlN interlayer with a growth rate of 0.006 nms^{-1} at 1000 °C with Cp_3Sc and 800 °C with $(MCp)_2ScCl$ as Sc precursor, respectively. The scan of a sample grown at 1000 °C without interlayer with Cp_3Sc as Sc precursor and a growth rate of 0.006 nms^{-1} is shown as a benchmark.

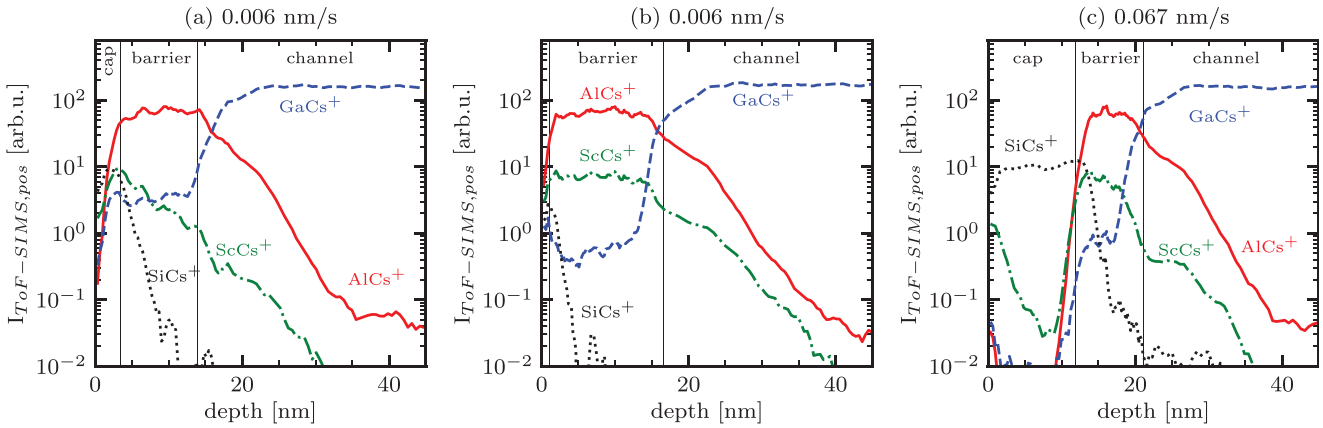

Figure 10. ToF-SIMS depth profiles of samples grown with AlN interlayer with a) Cp_3Sc at 1000 °C, b) $(MCp)_2ScCl$ at 800 °C with growth rates of 0.006 nms^{-1} and c) with $(EtCp)_2Sc(dtbt)$ at 1100 °C with a growth rate of 0.067 nms^{-1}. Obtained signals were normalized to NCs^+ signal to minimize the matrix effect. The oxidation layer developed on the surface of the SiN cap in (c) interferes with the $ScCs^+$ signal, and the signal in the first 10 nm belongs to $^{28}SiOHCs^+/^{29}SiOCs^+$. The $AlCs^+$ signal tail visible below approximately 7 x 10^{-2} arb. u. is a measurement artifact attributed to the background signal generated by sputter gun ions. The SiN_x and barrier including interlayer thicknesses determined by HRXRD are indicated by vertical lines.

grown on 4H-SiC. The number of thickness fringes of the heterostructure grown with $(EtCp)_2Sc(dtbt)$ on Al_2O_3 is however lower. This can be attributed to the increased amount of threading dislocations by the high lattice and thermal mismatch of Al_2O_3 and GaN. The HRXRD Θ/2Θ-scans of the samples grown with $(EtCp)_2Sc(dtbt)$ on the different substrates are shown in Figure S1 (Supporting Information).

3.2.1. Interface Abruptness

At low growth rates of 0.006 nms^{-1}, an AlN interlayer suppresses the formation of a linear AlGa(Sc)N grading at the interface. This is shown in **Figure 10**a,b. The sample grown with the Sc precursor Cp_3Sc and thus lower molar flow shows an increase in the $ScCs^+$ signal towards the SiN_x cap that corresponds to a Sc concentration increase from around 2.0 to 8.5 % (Figure 10a). The relatively high $GaCs^+$ signal background in the barrier layer indicates that a low amount of Ga is incorporated, which cannot be quantified due to the lack of SIMS standards. The increase in molar flow achieved with the Sc precursor $(MCp)_2ScCl$ allows for the growth of the barrier with homogeneous Sc incorporation (Figure 10b). The $GaCs^+$ signal background is reduced by one order of magnitude. $(EtCp)_2Sc(dtbt)$ as Sc precursor and a tenfold increase of the growth rate allows for the growth of a homogeneous barrier with low Ga background also at 1100 °C, as illustrated in Figure 10c. The diffusion tails of Al drop to the signal intensity of 10^{-1} within approximately 18 nm from the barrier/channel interface in both samples that were grown with a growth rate of 0.006 nms^{-1}. It seems that the growth temperature decrease from 1000 to 800 °C did not affect Al backdiffusion. With increased growth rate the diffusion tail was reduced by one quarter to around 14 nm even though the growth temperature

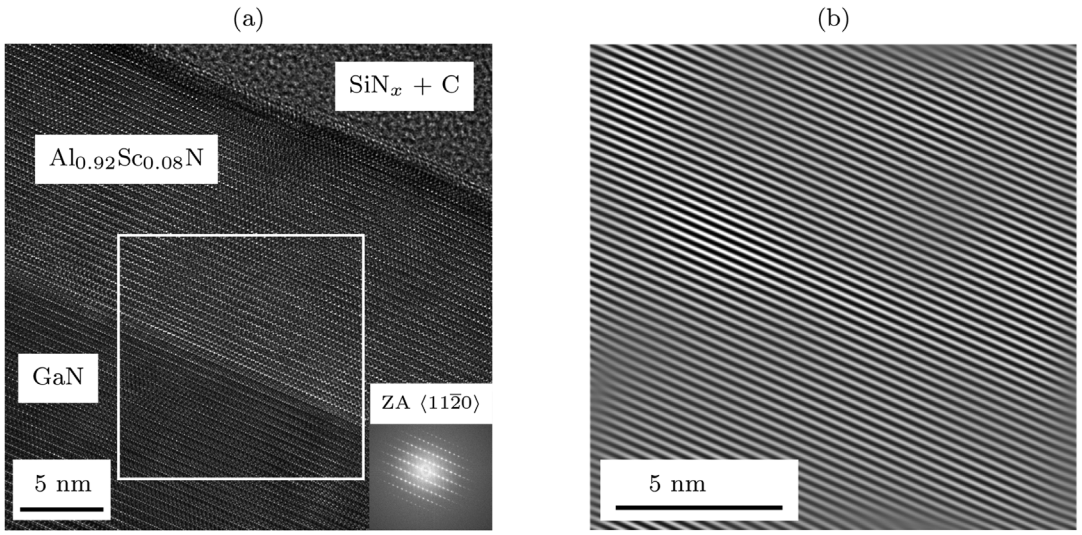

Figure 11. 15.5 nm - thick $Al_{0.92}Sc_{0.08}N$ barrier grown on GaN with an AlN interlayer at 800 °C. In (a) HRTEM and (b) Bragg filtered images taken along the ⟨11$\bar{2}$0⟩ - zone axis show superior structural quality.

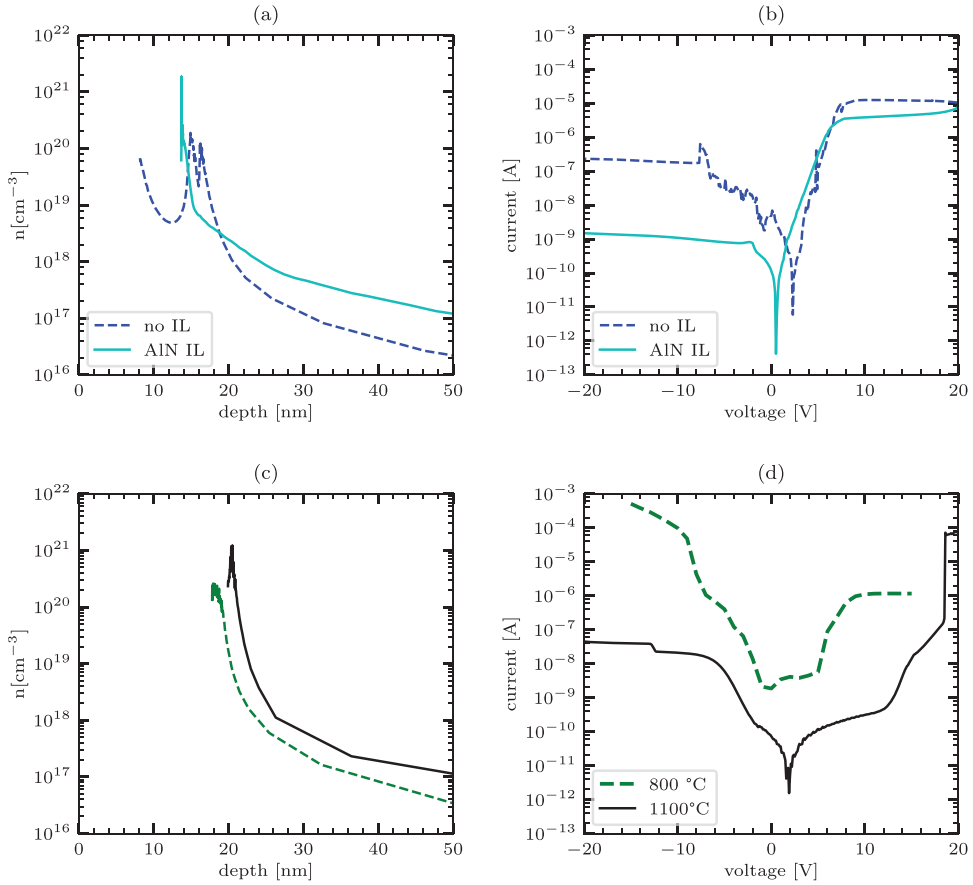

Figure 12. a) Charge carrier distribution across the depth profile of the samples grown with a growth rate of 0.006 nms^{-1} with Cp_3Sc as Sc precursor at 1000°C with and without nominal AlN interlayer and b) leakage current obtained by *I–V* measurement. c) Charge carrier distribution across the depth profile of the samples grown with interlayer using $(MCp)_2ScCl$ and a growth rate of 0.006 nms^{-1} at 800°C, and $(EtCp)_2Sc(dtbt)$ and a growth rate of 0.067 nms^{-1} at 1100 °C and d) leakage current obtained by *I–V* measurement.

was high with 1100 °C. Carbon and oxygen levels (not shown) are significantly higher for the samples grown at 800 °C than for those grown at 1200 °C, analog to the trends observed for GaN.[76]

In **Figure** 11a, the HRTEM image of the heterostructure grown at 800 °C with a growth rate of 0.006 nms^{-1} and nominal AlN interlayer with the Sc precursor $(MCp)_2ScCl$ is shown. The interface of the barrier and channel is very abrupt, and the contrast difference is clearly visible. One or two monolayers exhibit a higher contrast and can be attributed to the AlN interlayer. The interface and barrier are free of defects. No dislocations, stacking faults or cubic inclusions are visible. The Bragg filtered image in Figure 11b confirms this.

3.2.2. 2DEG Confinement

The charge carrier distribution obtained from the *C–V* measurements on the samples grown without and with interlayer at a growth rate of 0.006 nms^{-1} with Cp_3Sc are shown in **Figure** 12a. The sample grown without nominal interlayer shows a small parasitic capacitance increase at low positive voltages that translates to a spread of the 2DEG across the interlayer, confirming the presence of a broadened potential well and the formation of a 3DEG. The heterostructure grown with a nominal interlayer features no parasitic capacitance and the 2DEG seems well-confined. The leakage current shown in Figure 12b drops by two orders of magnitude from the low 10^{-7} to the low 10^{-9} A range with the insertion of a nominal AlN interlayer and increased interface abruptness. The mobility was found to decrease by 16 % from 957 to 802 cm^2(Vs)$^{-1}$ when a nominal AlN interlayer is inserted in heterostructures grown with Cp_3Sc,[27] and by 5 % from 914 to 868 cm^2(Vs)$^{-1}$ for the samples grown with $(EtCp)_2Sc(dtbt)$. This seems counterintuitive, as the AlN is expected to suppress alloy scattering and enhance electron mobility. Considering that the n_s increases from 2.52×10^{13} to 3.52×10^{13} (Cp_3Sc samples) and from 2.50×10^{13} to 2.64×10^{13} ($(EtCp)_2Sc(dtbt)$ samples), it can be assumed that increased electron–electron scattering is responsible for the mobility decrease. The growth temperature increase from 800 to 1100 °C does not show a strong effect on the charge carrier distribution determined from the *C–V* profile as shown in Figure 12c. In contrast, the *I–V* measurement Figure 12d reveals a very high leakage current in the 10^{-3} V range for negative voltages in the 800 °C-sample while that of the sample grown at 1100 °C is in the low 10^{-8} V range. We assume that the increased growth temperature suppresses impurity

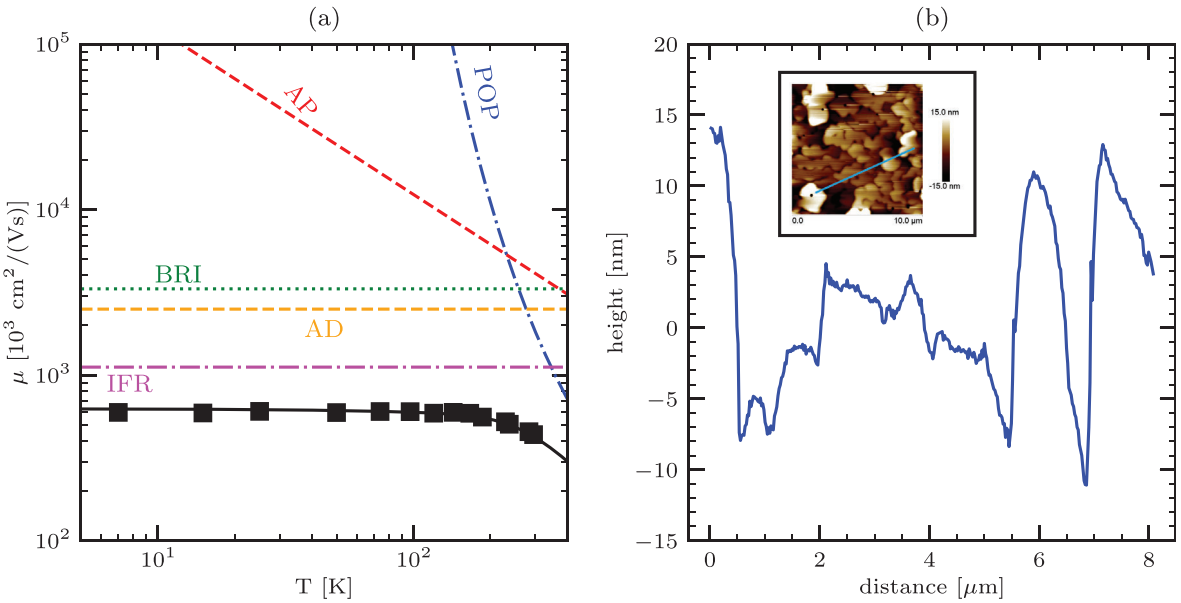

Figure 13. a) Electron mobility in the range of 7 to 270 K obtained by temperature-dependent Hall measurement on the sample grown at 800 °C with a growth rate of 0.006 nms^{-1} with AlN interlayer. At T < 200 K, the main -limiting mechanism is interface roughness scattering (IF) caused by the high surface roughness, shown in (b) the height profile obtained from the AFM 10x10 m^2 scan (inset). Other major –limiting mechanisms are background residual impurity (BRI) and alloy disorder (AD) scattering.

incorporation significantly and enhances the electrical performance.

3.2.3. Impact of Surface Roughness on the 2DEG

It remains surprising that the AlN interlayer, especially the well-defined one, grown at 800 °C and shown in Figure 11, hardly affects the mobility. Temperature-dependent Hall measurements show the typical behavior of a 2DEG, with higher mobility at low temperatures from 7 to 200 K and lower values at room temperature, as illustrated in **Figure 13a**. The mobility is surprisingly low with a value of approximately 595 $cm^2(Vs)^{-1}$. In literature, it has been observed that traps in the channel layer can be held responsible for low electron mobility, even more than atomically flat interfaces.[77] However, considering the high surface roughness of 7.82 nm observed by AFM in a 10 m^2 area, this low mobility is found to be related mainly to interface roughness scattering. The surface height profile obtained at a representative position is shown in Figure 13b. About 20 nm height differences are observed on a m-scale, which is in the range of the barrier thickness. This indicates that there are zones without 2DEG. Further, the polarization difference at the barrier/channel interface, that is responsible for the generation of the electric field that builds up across the barrier and generates the 2DEG, is sensitive to the barrier thickness. Accordingly, in regions of different barrier thicknesses, the electric field strength changes. This leads to fluctuations in the n_s and affects the electron mobility because electrons are deviated by different electric field strengths. Minor contributions to electron mobility are alloy scattering and background residual impurity scattering due to high oxygen and carbon levels. Low growth temperature seems to favor 3D growth.

4. Conclusion

In this work, we demonstrate that well-defined interfaces can be achieved in AlScN/GaN heterostructures grown by metal-organic chemical vapor deposition. The novel Sc precursors $(MCp)_2ScCl$, $(EtCp)_2Sc(bdma)$, and $(EtCp)_2Sc(dtbt)$, with their enhanced vapor pressures, allow for an increase of the growth rate by a factor of two, six, and ten, respectively, compared to the 0.006 nms^{-1} achieved with the conventional precursor Cp_3Sc. At low growth rates of 0.015 nms^{-1} and less, strain leads to the formation of linearly graded, quarternary interlayers with structural defects that broaden the potential well and the charge carrier distribution of the 2DEG. Abrupt interfaces and excellent structural quality are achieved with growth rates of 0.034 nms^{-1} and higher at growth temperatures of 1100 °C. At low growth rates of 0.006 nms^{-1}, excellent structural quality and homogeneous barriers are achieved when an AlN interlayer is inserted, the growth temperature is reduced to 800 °C, and the Sc molar flow increases with the precursor $(MCp)_2ScCl$. The electrical performance of the heterostructures is very sensitive to Sc accumulations at the cap/barrier interface, high surface roughness, and impurity incorporation at low growth temperatures. The most advantageous combination of structural quality and electrical performance was achieved when growing at a growth rate of 0.067 nms^{-1} with $(EtCp)_2Sc(dtbt)$ as a Sc precursor. HEMTs fabricated from such epilayers are expected to show considerably increased output power with respect to conventional AlGaN/GaN devices and the proof-of-concept AlScN/GaN devices fabricated so far.

Supporting Information

Supporting Information is available from the Wiley Online Library or from the author.

Acknowledgements

This work was funded by the BMBF Project ProMat_KMU "PuSH" Grant Number 03XP0387B. Dockweiler Chemicals GmbH supplied the Sc precursors for this study. GREMAN authors wish to thank GaN4AP (Gallium Nitride for Advanced Power Applications) project funded by the Electronic Component Systems for European Leadership Joint Undertaking (ECSEL JU), under grant agreement no.101007310. Further, the authors thank Nadine Brückner, Hanspeter Menner, Christian Manz, Stefan Müller, Timileyin Olanipekun, Barbara Weber, and Frank Bernhardt for their support with sample preparation and characterization. Jannis Jansen is gratefully acknowledged for setting up the tool for temperature-dependent Hall measurements. [Correction added on April 26, 2024, after first online publication: Dr. Stefano Leone has been marked as corresponding author in this version.]

Open access funding enabled and organized by Projekt DEAL.

Conflict of Interest

The authors declare no conflict of interest.

Data Availability Statement

The data that support the findings of this study are available from the corresponding author upon reasonable request.

Keywords

2D electron gas, AlScN, HRTEM, metal-organic chemical vapor deposition, vapor pressure

Received: February 19, 2024
Revised: April 9, 2024
Published online:

[1] R. Quay, P. Bruckner, A. Tessmann, E. Ture, D. Schwantuschke, M. Dammann, P. Waltereit, in 2017 Integrated Nonlinear Microwave and Millimetre-wave Circuits Workshop (INMMiC). IEEE, Piscataway NJ **2017**, pp. 1–3.
[2] E. Ture, S. Leone, P. Bruckner, R. Quay, O. Ambacher, 2019 IEEE MTT-S International Microwave Symposium (IMS), IEEE, Piscataway, NJ **2019**.
[3] M. Cwiklinski, P. Bruckner, S. Leone, C. Friesicke, R. Lozar, H. Massler, R. Quay, O. Ambacher, 2019 IEEE MTT-S International Microwave Symposium (IMS), IEEE, Piscataway, NJ **2019**.
[4] M. Cwiklinski, P. Bruckner, S. Leone, S. Krause, C. Friesicke, H. Massler, R. Quay, O. Ambacher, in 2020 IEEE/MTT-S International Microwave Symposium (IMS), IEEE, Piscataway, NJ **2020**, pp. 1117–1120.
[5] M. Meneghini, C. de Santi, I. Abid, M. Buffolo, M. Cioni, R. A. Khadar, L. Nela, N. Zagni, A. Chini, F. Medjdoub, G. Meneghesso, G. Verzellesi, E. Zanoni, E. Matioli, *J. Appl. Phys.* **2021**, *130*, 181101.
[6] F. Thome, P. Bruckner, S. Leone, R. Quay, in 2022 IEEE/MTT-S International Microwave Symposium - IMS 2022, IEEE, Piscataway, NJ **2022**, pp. 603–606.
[7] S. Leone, F. Benkhelifa, L. Kirste, C. Manz, R. Quay, O. Ambacher, *J. Appl. Phys.* **2019**, *125*, 23.
[8] I. Streicher, S. Leone, L. Kirste, C. Manz, P. Straňák, M. Prescher, P. Waltereit, M. Mikulla, R. Quay, O. Ambacher, *phys. status solidi (RRL) – Rapid Res. Lett.* **2022**, *17*, 2200387.
[9] F. Roccaforte, P. Fiorenza, G. Greco, R. Lo Nigro, F. Giannazzo, F. Iucolano, M. Saggio, *Microelectron. Eng.* **2018**, *187-188*, 66.
[10] D. F. Storm, D. A. Deen, D. S. Katzer, D. J. Meyer, S. C. Binari, T. Gougousi, T. Paskova, E. A. Preble, K. R. Evans, D. J. Smith, *J. Cryst. Growth* **2013**, *380*, 14.
[11] S. Leone, R. Fornari, M. Bosi, V. Montedoro, L. Kirste, P. Doering, F. Benkhelifa, M. Prescher, C. Manz, V. Polyakov, O. Ambacher, *J. Cryst. Growth* **2020**, *534*, 125511.
[12] P. Mazzolini, Z. Fogarassy, A. Parisini, F. Mezzadri, D. Diercks, M. Bosi, L. Seravalli, A. Sacchi, G. Spaggiari, D. Bersani, O. Bierwagen, B. M. Janzen, M. N. Marggraf, M. R. Wagner, I. Cora, B. Pécz, A. Tahraoui, A. Bosio, C. Borelli, S. Leone, R. Fornari, *Adv. Func. Mater.* **2023**, *33*, 2.
[13] M. T. Hardy, B. P. Downey, N. Nepal, D. F. Storm, D. S. Katzer, D. J. Meyer, *ECS Trans.* **2017**, *80*, 161.
[14] T. E. Kazior, E. M. Chumbes, B. Schultz, J. Logan, D. J. Meyer, M. T. Hardy, in 2019 IEEE MTT-S International Microwave Symposium (IMS), IEEE, Piscataway, NJ **2019**, pp. 1136–1139.
[15] O. Ambacher, B. Christian, M. Yassine, M. Baeumler, S. Leone, R. Quay, *J. Appl. Phys.* **2021**, *129*, 204501.
[16] O. Ambacher, A. Yassine, M. Yassine, S. Mihalic, E. Wade, B. Christian, *J. Appl. Phys.* **2022**, *131*, 24.
[17] M. Hardy, D. Meyer, N. Nepal, B. Downey, D. Scott Katzer, D. Storm, in 2018 IEEE MTT-S International Microwave Workshop Series on Advanced Materials and Processes for RF and THz Applications (IMWS-AMP), IEEE, Piscataway, NJ **2018**, pp. 1–3.
[18] S. Zhang, W. Y. Fu, D. Holec, C. J. Humphreys, M. A. Moram, *J. Appl. Phys.* **2013**, *114*, 243516.
[19] M. A. Moram, S. Zhang, *J. Mater. Chem. A* **2014**, *2*, 6042.
[20] D. V. Dinh, J. Lähnemann, L. Geelhaar, O. Brandt, *Appl. Phys. Lett.* **2023**, *122*, 152103.
[21] J. A. Del Alamo, E. S. Lee, *IEEE Trans. Electron Devices* **2019**, *66*, 4578.
[22] K. Frei, R. Trejo-Hernández, S. Schütt, L. Kirste, M. Prescher, R. Aidam, S. Müller, P. Waltereit, O. Ambacher, M. Fiederle, *Jpn. J. Appl. Phys.* **2019**, *58*, SC1045.
[23] C. Elias, M. Nemoz, H. Rotella, F. Georgi, S. Vézian, M. Hugues, Y. Cordier, *APL Mater.* **2023**, *11*, 031105.
[24] S. Leone, J. Ligl, C. Manz, L. Kirste, T. Fuchs, H. Menner, M. Prescher, J. Wiegert, A. Žukauskaitė, R. Quay, O. Ambacher, *phys. status solidi (RRL) – Rapid Res. Lett.* **2020**, *14*, 1900535.
[25] J. Ligl, S. Leone, C. Manz, L. Kirste, P. Doering, T. Fuchs, M. Prescher, O. Ambacher, *J. Appl. Phys.* **2020**, *127*, 195704.
[26] C. Manz, S. Leone, L. Kirste, J. Ligl, K. Frei, T. Fuchs, M. Prescher, P. Waltereit, M. A. Verheijen, A. Graff, M. Simon-Najasek, F. Altmann, M. Fiederle, O. Ambacher, *Semiconduct. Sci. Technol.* **2021**, *36*, 034003.
[27] I. Streicher, S. Leone, C. Manz, L. Kirste, M. Prescher, P. Waltereit, M. Mikulla, R. Quay, O. Ambacher, *Cryst. Growth Des.* **2023**, *23*, 782.
[28] S. Leone, P. Brueckner, L. Kirste, P. Doering, T. Fuchs, S. Mueller, M. Prescher, R. Quay, O. Ambacher, *phys. status solidi (b)* **2020**, *257*, 3.
[29] S. Leone, F. C. Beyer, A. Henry, O. Kordina, E. Janzén, *phys. status solidi (RRL) – Rapid Res. Lett.* **2010**, *4*, 305.
[30] S. Leone, F. C. Beyer, A. Henry, C. Hemmingsson, O. Kordina, E. Janzén, *Cryst. Growth Des.* **2010**, *10*, 3743.
[31] S. Leone, F. C. Beyer, H. Pedersen, S. Andersson, O. Kordina, A. Henry, E. Janzén, *Thin Solid Films* **2011**, *519*, 3074.
[32] N. Wolff, G. Schönweger, I. Streicher, M. R. Islam, N. Braun, P. Straňák, L. Kirste, M. Prescher, A. Lotnyk, H. Kohlstedt, S. Leone, L. Kienle, S. Fichtner, *Adv. Phys. Res.* **2024**, 2300113.
[33] D. Koleske, J. Knapp, S. Lee, M. Crawford, J. Creighton, K. Cross, G. Thaler, Issues associated with the metalorganic chemical vapor deposition of ScGaN and YGaN alloys, Springfield, VA **2009**, https://doi.org/10.2172/961650.

[34] C. Saidi, N. Chaaben, A. Bchetnia, A. Fouzri, N. Sakly, B. El Jani, *Superlattices Microstruct.* **2013**, *60*, 120.
[35] S. Bajaj, Z. Yang, F. Akyol, P. S. Park, Y. Zhang, A. L. Price, S. Krishnamoorthy, D. J. Meyer, S. Rajan, *IEEE Trans. Electron Devices* **2017**, *64*, 3114.
[36] A. Papamichail, A. R. Persson, S. Richter, P. Kühne, V. Stanishev, P. O. Å. Persson, R. Del Ferrand-Drake Castillo, M. Thorsell, H. Hjelmgren, P. P. Paskov, N. Rorsman, V. Darakchieva, *Appl. Phys. Lett.* **2023**, *122*, 153501.
[37] L. Shen, S. Heikman, B. Moran, R. Coffie, N.-Q. Zhang, D. Buttari, I. P. Smorchkova, S. Keller, S. P. DenBaars, U. K. Mishra, *IEEE Electron Dev. Lett.* **2001**, *22*, 457.
[38] J. Casamento, T.-S. Nguyen, Y. Cho, C. Savant, T. Vasen, S. Afroz, D. Hannan, H. Xing, D. Jena, *Appl. Phys. Lett.* **2022**, *121*, 192101.
[39] E. Dogmus, R. Kabouche, S. Lepilliet, A. Linge, M. Zegaoui, H. Ben-Ammar, M.-P. Chauvat, P. Ruterana, P. Gamarra, C. Lacam, M. Tordjman, F. Medjdoub, *Electronics* **2016**, *5*, 31.
[40] D. Cai, X. Chen, H. Xu, N. Lin, F. Xu, H. Chen, *Jpn. J. Appl. Phys.* **2013**, *52*, 08JB30.
[41] L. Calcagno, G. Izzo, G. Litrico, G. Foti, F. La Via, G. Galvagno, M. Mauceri, S. Leone, *J. Appl. Phys.* **2007**, *102*, 4.
[42] S. Leone, H. Pedersen, A. Henry, O. Kordina, E. Janzén, *Mater. Sci. Forum* **2008**, *600–603*, 107.
[43] F. La Via, G. Galvagno, F. Roccaforte, F. Giannazzo, S. Di Franco, A. Ruggiero, R. Reitano, L. Calcagno, G. Foti, M. Mauceri, S. Leone, G. Pistone, F. Portuese, G. Abbondanza, G. Abbagnale, A. Veneroni, F. Omarini, L. Zamolo, M. Masi, G. L. Valente, D. Crippa, *Microelectron. Eng.* **2006**, *83*, 48.
[44] S. Leone, A. Henry, E. Janzén, S. Nishizawa, *J. Cryst. Growth* **2013**, *362*, 170.
[45] S. Leone, F. C. Beyer, H. Pedersen, O. Kordina, A. Henry, E. Janzén, *Mater. Res. Bull.* **2011**, *46*, 1272.
[46] S. Leone, O. Kordina, A. Henry, S.-i. Nishizawa, Ö. Danielsson, E. Janzén, *Cryst. Growth Des.* **2012**, *12*, 1977.
[47] A. Henry, S. Leone, F. C. Beyer, H. Pedersen, O. Kordina, S. Andersson, E. Janzén, *Phys. B: Condens. Matter* **2012**, *407*, 1467.
[48] S. Krause, I. Streicher, P. Waltereit, L. Kirste, P. Bruckner, S. Leone, *IEEE Electron Dev. Lett.* **2023**, *44*, 17.
[49] A. J. Green, J. K. Gillespie, R. C. Fitch, D. E. Walker, M. Lindquist, A. Crespo, D. Brooks, E. Beam, A. Xie, V. Kumar, J. Jimenez, C. Lee, Y. Cao, K. D. Chabak, G. H. Jessen, *IEEE Electron Dev. Lett.* **2019**, *40*, 1056.
[50] A. J. Green, N. Moser, N. C. Miller, K. J. Liddy, M. Lindquist, M. Elliot, J. K. Gillespie, R. C. Fitch, R. Gilbert, D. E. Walker, E. Werner, A. Crespo, E. Beam, A. Xie, C. Lee, Y. Cao, K. D. Chabak, *IEEE Electron Dev. Lett.* **2020**, *41*, 1181.
[51] K. Kobayashi, V. Kumar, A. Xie, J. Jimenez, E. Beam, A. Ketterson, IEEE MTT-S International Microwave Symposium (IMS) **2021**, pp. 772–775.
[52] M. B. Tahhan, J. A. Logan, M. T. Hardy, M. G. Ancona, B. Schultz, B. Appleton, T. Kazior, D. J. Meyer, E. M. Chumbes, *IEEE Trans. Electron Dev.* **2022**, *69*, 962.
[53] S. Leone, I. Streicher, M. Prescher, P. Straňák, L. Kirste, *phys. status solidi (RRL) – Rapid Res. Lett.* **2023**, *17*, 2300091.
[54] DOCKWEILER CHEMICALS, Dockweiler Chemicals, https://dockchemicals.com/ (accessed: August 2022).
[55] S. Leone, F. Benkhelifa, L. Kirste, C. Manz, S. Mueller, R. Quay, T. Stadelmann, *phys. status solidi (b)* **2018**, *255*, 1700377.
[56] F. C. Beyer, C. G. Hemmingsson, S. Leone, Y.-C. Lin, A. Gällström, A. Henry, E. Janzén, *J. Appl. Phys.* **2011**, *110*, 12.
[57] D. Wang, D. Wang, P. Zhou, M. Hu, J. Liu, S. Mondal, T. Ma, P. Wang, Z. Mi, *Appl. Surf. Sci.* **2023**, *628*, 157337.
[58] A. Zukauskaite, G. Wingqvist, J. Palisaitis, J. Jensen, P. O. Å. Persson, R. Matloub, P. Muralt, Y. Kim, J. Birch, L. Hultman, *J. Appl. Phys.* **2012**, *111*, 093527.
[59] O. Ambacher, J. Smart, J. R. Shealy, N. G. Weimann, K. Chu, M. Murphy, W. J. Schaff, L. F. Eastman, R. Dimitrov, L. Wittmer, M. Stutzmann, W. Rieger, J. Hilsenbeck, *J. Appl. Phys.* **1999**, *85*, 3222.
[60] P. Fay, D. Jena, P. Maki, editors, *High-Frequency GaN Electronic Devices*, Springer International Publishing, Cham **2020**.
[61] C. Wood, D. Jena, *Polarization effects in semiconductors: From ab initio theory to device application*, Springer, New York **2008**.
[62] D. Jena, *Quantum physics of semiconductor materials and devices*, Oxford scholarship online. Oxford University Press, Oxford, NY **2022**.
[63] S. Birner, nextnano - Software for semiconductor nanodevices, https://www.nextnano.de/ (accessed: August 2022).
[64] J. Bai, T. Wang, P. J. Parbrook, K. B. Lee, Q. Wang, A. G. Cullis, in *Microscopy of Semiconducting Materials 2007*, 33–36. Springer, Dordrecht **2008**.
[65] J. A. Floro, D. M. Follstaedt, P. Provencio, S. J. Hearne, S. R. Lee, *J. Appl. Phys.* **2004**, *96*, 7087.
[66] C. Bazioti, E. Papadomanolaki, T. Kehagias, T. Walther, J. Smalc-Koziorowska, E. Pavlidou, P. Komninou, T. Karakostas, E. Iliopoulos, G. P. Dimitrakopulos, *J. Appl. Phys.* **2015**, *118*, 15.
[67] J. Moneta, E. Grzanka, H. Turski, C. Skierbiszewski, J. Smalc-Koziorowska, *Semiconduct. Sci. Technol.* **2020**, *35*, 034003.
[68] I. G. Vasileiadis, I. Belabbas, C. Bazioti, J. Smalc-Koziorowska, P. Komninou, G. P. Dimitrakopulos, *phys. status solidi (b)* **2021**, *258*, 2100190.
[69] C. Stampfl, C. G. van de Walle, *Phys. Rev. B* **1998**, *57*, R15052.
[70] G. P. Dimitrakopulos, C. Bazioti, E. Papadomanolaki, K. Filintoglou, M. Katsikini, J. Arvanitidis, E. Iliopoulos, *Mater. Sci. Technol.* **2018**, *34*, 1565.
[71] F. Meng, M. Estruga, A. Forticaux, S. A. Morin, Q. Wu, Z. Hu, S. Jin, *ACS Nano* **2013**, *7*, 11369.
[72] A. C. Lang, J. L. Hart, J. G. Wen, D. J. Miller, D. J. Meyer, M. L. Taheri, *Appl. Phys. Lett.* **2016**, *109*, 13.
[73] K. R. Talley, S. L. Millican, J. Mangum, S. Siol, C. B. Musgrave, B. Gorman, A. M. Holder, A. Zakutayev, G. L. Brennecka, *Phys. Rev. Mater.* **2018**, *2*, 063802.
[74] Z. Liu, X. Wang, X. Ma, Y. Yang, D. Wu, *Appl. Phys. Lett.* **2023**, *122*, 122901.
[75] J. S. Cetnar, A. N. Reed, S. C. Badescu, S. Vangala, H. A. Smith, D. C. Look, *Appl. Phys. Lett.* **2018**, *113*, 192104.
[76] J.-T. Chen, U. Forsberg, E. Janzén, *Appl. Phys. Lett.* **2013**, *102*, 193506.
[77] A. Hospodková, F. Hájek, T. Hubáček, Z. Gedeonová, P. Hubík, M. Hývl, J. Pangrác, F. Dominec, T. Košutová, *ACS Appl. Mater. Interfaces* **2023**, *15*, 19646.